View metadata, citation and similar papers at core.ac.uk
brought to you by CORE
provided by AIR Universita degli studi di Milano

High-pressure behavior and phase stability of $Na_2B_4O_6(OH)_2 \cdot 3H_2O$ (kernite)

Davide Comboni[1,2*], Francesco Pagliaro[1], G. Diego Gatta[1], Paolo Lotti[1], Sula Milani[1], Marco Merlini[1], Tommaso Battiston[1], Konstantin Glazyrin[3], Hanns-Peter Liermann[3]

[1] Dipartimento di Scienze della Terra, Università degli Studi di Milano, Via Botticelli 23, 20133 Milano, Italy

[2] ESRF − European Synchrotron Radiation Facility, 71 Avenue des Martyrs, CS40220, 38043 Grenoble Cedex, France

[3] Photon Sciences, DESY, PETRA-III, Notkestrasse 85, D-22607, Hamburg, Germany

* **Corresponding Author:** Davide Comboni, current email address davide.comboni@esrf.fr

Abstract

The high-pressure behavior of kernite [ideally $Na_2B_4O_6(OH)_2 \cdot 3H_2O$, a ~7.02 Å, b ~9.16 Å, c ~15.68 Å, β = 108.9°, Sp. Gr. $P2_1/c$, at ambient conditions], an important B-bearing raw material (with B_2O_3 ≈ 51 wt%) and a potential B-rich aggregate in radiation shielding materials, has been studied by single-crystal synchrotron X-ray diffraction up to 14.6 GPa. Kernite undergoes an iso-symmetric phase transition at 1.6 – 2.0 GPa (to kernite-II). Between 6.6 -7.5 GPa, kernite undergoes a second phase transition, possibly iso-symmetric in character (to kernite-III). The crystal structure of kernite-II was solved and refined. The isothermal bulk modulus ($K_{V0} = \beta^{-1}_{P0,T0}$, where $\beta_{P0,T0}$ is the volume compressibility coefficient) of the ambient-pressure polymorph of kernite was found to be K_{V0} = 29(1) GPa and a marked anisotropic compressional pattern, with $K(a)_0 : K(b)_0 : K(c)_0$ ~ 1:3:1.5., was observed. In kernite-II, the K_{V0} increase to 43.3(9) GPa and the anisotropic compressional pattern increases pronouncedly. The mechanisms, at the atomic scale, which govern the structure deformation, have been described.

Keywords: borates; X-ray methods; single crystals; phase-transitions; high-pressure

1. Introduction

Natural borates are the most important source of boron, an important geochemical marker (in particular in pegmatitic and granitic systems) for petrogenetic processes and a strategic element in a series of technological processes. Nowadays, although borates are used in more than 300 different

applications, more than 75% of world consumption is due to the production of ceramics, detergents (in particular boric acid), fertilizers, and glass [1]. Borates are also being used for the production of radiation-shielding materials because of the ability of ^{10}B, which accounts for *ca.* 20% of the natural boron, to absorb thermal neutrons, due to its high cross section, for the $^{10}B(n,\alpha)^{7}Li$ reaction (~3840 barns) [2, 3]. Borates could be added to concretes or epoxy resins in order to enhance the shielding efficiency towards neutron radiations [4–7].

Among the B-bearing minerals, colemanite, kernite, borax, and ulexite account for about 90% of the borate raw materials used worldwide. Kernite, ideally [$Na_2B_4O_6(OH)_2 \cdot 3H_2O$], named after a large ore deposit in Kern County (CA, USA), was discovered in the Mojave Desert, near the modern town of Boron, California, in 1925 and was originally named "rasorite" [8]. Because of its low density (1.9 g/cm^3), kernite could be utilised for the production of lightweight concretes, although the use of kernite as B-rich aggregate in Portland cements concretes is ultimately hindered by its high sodium content (Na_2O 21.3 wt%). Sodium could promote deleterious reactions for the durability of Portland cements (*e.g.*, "alkali-silica reactions" – ASR). However, the role of Na and B in Sorel cements (*i.e.*, magnesium oxychloride cements), is still unknown. Sorel cements are not used in reinforced concretes, due to their incompatibility with steel reinforcement because of the presence of chlorine. Instead, they are commonly used to make floor tiles and panels for fire protection. In this light, B-additivated Sorel cements could be efficiently used for the production of radiation-shielding tiles or panels. Therefore, a detailed characterization of the structure-property relationships of borates is advisable and kernite, which is a relatively low-cost natural commodity, represents a potentially good candidate.

The mineral kernite belongs to the sodium borate series $Na_2O \cdot 2B_2O_3 \cdot nH_2O$, whose known members are with n = 0, 1, 2 (metakernite), 3 (kernite), 5 (tincalconite) and 10 (borax) [9]. The structure of kernite is constructed by two (crystallographically independent) triangular BO_2OH groups and two tetrahedral BO_4 groups, which form 3-fold rings by sharing corner-bridging O atoms, and $NaO_4(OH)(OH_2)$ and $NaO_2(OH)(OH_2)_3$ polyhedra. The majority of the O sites are involved in H-bonding, as donors or as acceptors, suggesting that the H-bonding network in the structure of this borate is pervasive and play an important role on its structural stability. A recent study by Gatta et al. [10] shed new light on the H-disorder in the structure of kernite, on the basis of single-crystal neutron diffraction data. A few studies were devoted to investigate the stability of kernite under ambient pressure conditions [11–13]. When heated in air, above ~353 *K*, kernite dehydrates to $Na_2B_4O_6(OH)_2 \cdot 1.5H_2O$; at T >388 *K* it becomes amorphous and, at temperature above ~800 *K*, an anhydrous phase with composition $Na_2B_4O_7$ crystallizes [12]. However, only one high-pressure study explored the *P*-induced behavior of kernite *via* Raman and IR spectroscopy by *in-situ* experiments [14].

Silva et al. [14] detected three potential phase transitions occurring at about 2.5, 7.0 and 11.0 GPa, suggesting a series of changes concerning the bonding configuration of Na-polyhedra and the BO_3 and BO_4 groups. To the best of our knowledge, no *in-situ* X-ray diffraction experiments were devoted to unveil the high-pressure behavior mechanisms that govern the structure deformation at the atomic scale, driving the *P*-induced phase transitions of kernite described by Silva et al. [14]. Furthermore, the compressional parameters of kernite (and those of its high-pressure polymorphs) are still unknown, which might be very relevant when using kernite as source for radiation-shielding tiles (*e.g.,* impact resistance). For these reasons, we investigated the high-pressure behavior of kernite by *in-situ* single-crystal X-ray diffraction up to 14.5 GPa under quasi-hydrostatic conditions, in order to obtain the compressional-elastic parameters and the *P*-induced stability fields which, along with the *T*-data previously published, will provide a clear picture of the *P-T* response of this B-bearing material. A comprehensive characterization of the crystal-chemistry, elastic properties, stability and structural behaviors of natural borates at varying *T* and *P* conditions is fundamental for modelling and understanding their role when adopted as aggregates in concretes.

2. Experimental procedures

A sample of kernite from the Kramer Deposit, Mohave Desert, Kern County, California [11, 15], was used in this study. More details about the occurrence of the sample were recently reported by Gatta et al. [10]. Its chemical composition, obtained on the basis of a multi-methodological approach (*i.e.*, titrimetric and gravimetric analysis for the determination of the Na_2O and B_2O_3 content, thermogravimetric measurements to assess the H_2O content, ICP-AES analysis for minor elements), led to a general experimental formula of $Na_{1.99}B_{3.99}O_6(OH)_2 \cdot 3.01H_2O$, close to the ideal formula of kernite. A crystal with size ~ 50 × 40 × 20 μm^3 was selected for the X-ray diffraction experiment. *In-situ* high-pressure single-crystal synchrotron X-ray diffraction experiment was performed at the Extreme Conditions Beamline P02.2 at PETRA-III/DESY. A wavelength ~0.2897 Å (photons with energy ~42.7 keV) was used, with a focusing spot of ~8.5 (H) x 1.8 (V) μm^2, originating from a compound refractive lenses (CRL) system consisting of 111 Be lenses with a radius of 50 μm (380 μm beam acceptance) and a focal length of 1.221 mm. Preliminary experiments showed a severe reaction of kernite with the commonly used methanol-ethanol mixtures as *P*-transmitting fluid. Due to its high solubility in polar solvents, neon was used as quasi-hydrostatic pressure-transmitting medium [16]; no evidence of interaction with Ne was observed. The crystal of kernite was loaded in a symmetric diamond anvil cell (DAC), equipped with Boehler–Almax design diamonds/seats with a (nominal) 70° opening and 300-μm culets size. A 250-μm-thick rhenium gasket was pre-indented to 50 μm and then drilled to form a 150 μm hole, in which the kernite crystal, along with the pressure

calibrant (ruby spheres [17]), were placed. Pressure was increased with an automated pressure-driven system and measured with the online ruby/alignment system, after an average equilibration time of 15 minutes. Diffraction images were acquired on a PerkinElmer XRD 1621 flat panel detector, using an in-house script for collecting step-scan diffraction images. Sample to detector distance (402.34 mm) was calibrated using a CeO_2 standard (NIST 674a) and an enstatite ($MgSiO_3$) crystal. The diffraction images were then converted to conform to the "Esperanto" format of the program CrysAlis [18, 19]. X-ray diffraction data were first collected at ambient pressure with the crystal in the DAC without the pressure-transmitting fluid. The data collection strategy consisted in a pure ω-scan ($-32° \leq \omega \leq +32°$), with a step size of 0.5° and an exposure time of 1 s/frame. X-ray diffraction peaks were indexed and their intensities were integrated and corrected for Lorentz-polarization effects, using the CrysAlis package [19]. Scaling and correction for absorption (due to the DAC components) was applied by the semi-empirical *ABSPACK* routine implemented in CrysAlis. The same data collection strategy was used for the high-pressure measurements. High-pressure data collections were performed about 30 minutes after each *P*-increase, in order to stabilize the pressure conditions. At *P* above 8-9 GPa, due to a significant decrease of the diffraction peak's intensity, the exposure time was increased to 3 s/frame. Selected diffraction patterns are shown in Fig. 1. The unit-cell parameters at high pressure are listed in Table 1 and their evolution with *P* is shown in Fig. 2.

3. Structure refinement protocol and elasticity analysis

All the structure refinements were performed using the package JANA2006 [20]. For the low-pressure polymorph, the H-free structure reported by Cooper et al. [9] was used as starting model. In order to increase the quality of the structure refinements, the displacement parameters (D.P.) of selected sites were refined as anisotropic (see Table S1, Supplementary materials, SM). No restraints on bond distances or angles were used. Between 1.6 and 2.0 GPa, kernite experienced the first iso-symmetric phase transition to the kernite-II polymorph; the structure of kernite-II was successfully solved by the *Superflip* software [21], implemented in JANA2006. The refinement, providing the best figure of merit, was conducted modelling Na1 and Na2 sites as anisotropic, and all the other atomic sites as isotropic. Also in this case, no restraints were adopted. A second phase transition, likely iso-symmetric, to the kernite-III polymorph occurred between 6.6 and 7.5 GPa. Unfortunately, an abrupt drop in intensity and number of observed reflections hindered the structure solution of the kernite-III structure.

Atomic coordinates, site occupancy factors and displacement parameters of the structure refinements are given in Table S1 (SM). The principal statistical parameters of the structure refinements are listed in Table S2 (SM). Relevant inter-atomic angles and distances are reported in

Tables 2 and 3. Other interatomic distances pertaining to the BO_x groups are listed in Table S3. CIFs (crystallographic information files) pertaining to the structures of kernite-I and -II have been deposited as supplementary material.

The compressional behavior of kernite was described by fitting the *P*-*V* data to a second-order Birch-Murnaghan Equation of State (BM-EoS), using the EOS-FIT software [22, 23]. This isothermal EoS is based on the assumption that the high-pressure strain energy in a solid can be expressed as a Taylor series in the Eulerian finite strain, defined as:

$$fe = [(V_0/V)^{2/3} - 1]/2,$$

and allows to refine the bulk modulus (K_{V0} or $K_{P0,T0} = -V_0(\partial P/\partial V)_{T0} = \beta^{-1}_{P0,T0}$, where $\beta_{P0,T0}$ is the volume compressibility coefficient at room conditions) and its *P*-derivatives. Expansion in the Eulerian strain polynomial has the following form:

$$P(fe) = 3K_{P0,T0}\, fe\, (1 + 2fe)^{5/2} \{1 + 3/2(K' - 4)fe + 3/2[K_{P0,T0}K'' + (K' - 4)(K' - 3) + 35/9]\, fe^2 + ...\},$$

where $K' = \partial K_{P0,T0}/\partial P$ and $K'' = \partial^2 K_{P0,T0}/\partial P^2$.

Truncated to the second order in energy, $K' = \partial K_{P0,T0}/\partial P = 4$ and the EoS transforms to:

$$P(fe) = 3K_{P0,T0}\, fe\, (1 + 2fe)^{5/2}.$$

The analysis of the *fe*-*F*e plot [22, 23] (where *F*e is the normalised pressure, defined as $Fe = P/3fe(1+2fe)^{5/2}$) reveals that the truncation to the second-order polynomial provides the best figure of merit for all the polymorphs. Data were fitted taking into account an estimated uncertainty of ± 0.05 GPa for pressure, as commonly determined adopting the ruby fluorescence method for *P*-calibration [17]. The BM-EoS parameters, refined minimizing the difference between the EoS curve and the experimental data (weighted by their uncertainties in *P* and *V*), are listed in Table 4.

4. Results and discussion

4.1 Compressional behavior

The evolution of the unit-cell parameters of kernite with pressure (shown in Fig. 2 and listed in Table 1) appears to be monotonic up to 1.6 GPa, where a first phase transition (from kernite to kernite-II) occurs. Comparing the unit-cell volume of the low-*P* polymorph at 1.60(5) GPa and that of kernite-II at 2.00(5) GPa, a difference of about 7.5% is observed. The transformation is, therefore, a first-order phase transition. This phase transition is not followed by a change in the space group, which remains $P2_1/c$ (as suggested by the reflection conditions); structural changes induced by the phase transition will be described in the next section. In response to the first phase transition, the unit-cell edges parallel to *a* and *b* increase by about 1.7 and 1.4%, respectively, whereas that along *c* decreases by almost 8.2%. In the low-*P* polymorph, the monoclinic β angle progressively increases from 108.87(2)° at ambient pressure to 110.16(2)° at 1.60(5) GPa (Fig. 2, Table 1). After the first

phase transition, the β angle experiences a drastic rise to 114.49(3)°; further pressure increase leads to a slight increment of its value, up to 115.19(2)° at 6.56(5) GPa (Fig. 2, Tab. 1). The compressional behavior of the unit-cell volume (and along the principal crystallographic directions) appears to be monotonic up to 6.56(5) GPa, where the second phase transition (kernite-II-to-kernite-III) occurs. Also in this case, the transformation can be described as a first-order phase transition, with unit-cell volume decrease of about 7%. The space group seems to be preserved, though a drastic reduction of both data quality and number of Bragg reflections (Fig. 1) ultimately hindered the crystal structure solution of the kernite-III polymorph, leaving ambiguity about its actual space group. Interestingly, the *b* and *c* unit-cell edges after a first decrease (see Fig. 2 and Table 1) experience an additional drop at ~8.3 GPa. On the other hand, the unit-cell edge parallel to *a* seems to increase after this initial stage. Unfortunately, without structural data, it is impossible to assess if this behavior is due to the occurrence of a third phase transition or if it is due to a transient behavior connected to the kernite-II-to-kernite-III phase transition.

All the polymorphs of kernite display an interesting anisotropic behavior (Table 4 and S4). Ambient-pressure kernite polymorph is a relatively soft mineral (K_{V0} ~29 GPa) with a pronounced anisotropy scheme, being $K(a)_0 : K(b)_0 : K(c)_0$ ~ 1:3:1.5. After the first phase transition, between 1.6 and 2.0 GPa, the bulk modulus increases to ~44 GPa. However, if its increment in kernite-II is rather unimpressive, the change in its anisotropic scheme is drastic: while the compressibility along *a* is practically unaffected by the phase transition, $K(c)$ increases by 50% and $K(b)$ almost triples (from 66 to 175 GPa, Table 4). After the kernite-II-to-kernite-III phase transition, between 6.5 and 7.5 GPa, the bulk modulus of kernite-III drops down to 36(3) GPa. In this polymorph, while $K(b)$ was impossible to determine due to the scattering of the *b*-*P* data (Table 1, Fig. 2), $K(c)$ drops from 49 to 21 GPa and $K(a)$ is 4 GPa only, an unrealistic value affected by a large relative uncertainty (± 2 GPa), which highlights that the structure is very stressed and likely unstable. This is rather interesting and the structural reasons behind this behavior will be discussed in the next section. Data collected in decompression show a significant hysteresis loop, as kernite-III survives (at least) down to 4.50(5) GPa and kernite-II down to 1.20(5) GPa (Table 1 and Fig. 2). Eulerian strain analyses were performed with the *Win_Strain* software [24] in order to describe magnitude and orientation of the unit-strain ellipsoid for the three kernite polymorphs. The results, shown in Table S4, confirm that the direction of the lower compressibility is parallel to the [010] crystallographic axis in all the three polymorphs, and the anisotropic compressional scheme of kernite and kernite-II is highly pronounced.

4.2. Deformation mechanisms and phase transitions

Up to 1.60(5) GPa, no dramatic changes occur in the crystal structure of kernite. However, some relevant modifications, regarding a few inter-atomic distances, are critical in order to fully understand the deformation mechanisms that drive the first *P*-induced phase transition. The B-O units are substantially uncompressible (as expected at low pressure), along with most of the Na-O distances (*e.g.*, Na2-O4 and Na2-O11 decrease only by about 0.05Å and 0.03Å, respectively). However, some other distances pertaining to the Na2 and Na1 coordination polyhedra show a significant decrease: Na2-O6, Na1-O8 and Na1-O7 decrease from 3.114(4) to 2.930(8) Å, from 4.258(3) to 4.099(6)Å and from 4.025(2) to 3.909(4)Å, respectively (see Table 3). Although it might seem that such a decrease is only marginal, these modifications are expected to drive the first *P*-induced phase transition, occurring at relatively low-*P* (between 1.6 and 2.0 GPa).

The kernite-to-kernite-II phase transition is a first-order transformation, and it is reconstructive in character. In order to describe the major structural modifications in response to the phase transition, we followed the evolution experienced by the O2-O4-O9 and O1-O4-O2 angles (Fig. 3, Table 2): O2-O4-O9 increases from 89.3(1)° to 124.5(2)°, whereas O1-O4-O2 decreases from 147.0(2) to 111.8(2)°. These changes deeply affect the coordination environments of the Na2- and Na1-polyhedra, which increase their coordination number to CN=VII. At ambient pressure, Na2 is 5-fold (or 5 + 1) coordinated with three O atoms (O1, O4, O6) and two H_2O molecules (*i.e.*, O11 and two O10), while Na1 is 6-fold coordinated with five O atoms (O6, O4, O9, O2 and O3) and one H_2O molecule (O8). At *P*>1.6 GPa, due to the decrease of the O1-O4-O2 angle, O2 enters the coordination environment of Na2 (Na2-O2 ~ 2.5Å). Moreover, the distance Na2-O6 sharply decreases from 2.930(8) to 2.533(8) Å (Table 3). These deformation mechanisms increase the coordination of Na2 from V to VII. On the other hand, due to the changes in the aforementioned angles, the Na1-polyhedron rotates anticlockwise on the *bc* plane, leading to two main effects (Fig. 3). In response to the distance reduction between the BO_3/BO_4 chains and the Na1-polyhedron, each O8 site enters also in the coordination environment of the farthest Na1 site. In fact, at ambient pressure, O8 is at ~2.30 Å to the closest Na1 site and at ~4.26 Å to the farthest one (Tab. 3, Fig. 3). These distances change slightly in the low-*P* regime (*i.e.*, at 1.6 GPa the distances are ~2.25 and ~4.10 Å, respectively). However, in response to the kernite-to-kernite-II phase transition, one increases from 2.25 to 2.53 Å whereas the other decreases from 4.10 to 2.37 Å. In addition, because of the rotation, Na1 approaches also the position of the O7 site. In fact, at 1.6 GPa, the distance Na1-O7 is 3.90 Å, whereas at 2.00 GPa Na1-O7 drops to 2.46 Å. However, the anticlockwise rotation moves away Na1 from O9 (Fig. 3), increasing the Na1-O9 distance from 2.41 to 3.18 Å (Tab. 3). Moreover, as shown in Table 3, the phase transition leads to a change in the bonding configuration between Na1 and O6. Two symmetry-

equivalents O6, at 1.60(5) GPa, lie respectively at 2.376(7) Å and 3.861(5) Å from Na1 (Fig. 3). In Fig. 3, the O6 site belonging to the coordination environment of Na1, in the low-*P* polymorph structure and in kernite-II, is marked with an asterisk (*), whereas the farthest O6 site is shown without. After the phase transition, Na1-O6* increases from 2.376(7) Å to 2.869(7) Å, whereas Na1-O6 slightly decreases from 3.858(8) Å to 3.795(10) Å. The aforementioned changes overall increase the coordination number of Na1 from VI to VII, but with a significant rearrangement of its coordination environment. The Na1-anticlockwise rotation on the *bc* plane, coupled with the changes of the O1-O4-O2 and O2-O4-O9 angles, reduce the gap along the [001] direction between the BO_4/BO_3 chains, resulting into the abrupt contraction of the *c* unit-cell edge. Moreover, the tilting of the BO_4 units (Tab. 3) gives rise to a BO_4/BO_3 chains stretching on the [010] direction, with a consequent increase of the *b* unit-cell parameter (Fig. 2 and 3).

The increase of the Na coordination numbers also changes drastically the connection between the different Na-polyhedra. At ambient pressure, O4 is the bridging oxygen between Na2- and Na1-polyhedra, while two O10 are edge-shared between Na2-polyhedra, with a zig-zig configuration shown in Fig. 4. After the phase transition, the Na-polyhedra are all connected by edge sharing, to form continuous ribbons and, ultimately, a complex system of elliptical 10-membered rings (hereafter 10-mRs), made by 5 Na2- and 5 Na1-polyhedra (Fig. 4). Quite interesting, in kernite-II, the H_2O oxygen site O8 connects two adjacent Na1 polyhedra, allowing the formation of the continuous Na-polyhedra ribbons (Fig. 4). The same role may be observed in the case of the other H_2O O10 site, in kernite and in kernite-II (see Fig. 3 and 4). Unfortunately, in high-pressure experiments it is impossible to locate H atoms, due to their poor X-ray scattering cross-section. In this light, any change on the proton location and H- bonding configuration cannot be described.

In kernite-II, the B-O distances do not vary significantly, except for B4-O6 which drops from 1.37(1) Å (at 5.83(5) GPa) to 1.31(2)Å (at 6.56(5) GPa). These findings indicate that also at these pressures the BO_X units act as rigid bodies, at a first approximation. The sharp change in the B4-O6 distance at 6.5 GPa could reflect the (second) impending phase transition, which is bracketed between 6.56(5) GPa and 7.51(5) GPa. Considering the evolution of the bonding configuration of the two independent Na-polyhedra, significant changes occur in kernite-II at high pressure. Into details, Na2-O11, Na2-O10 and Na2-O6 decrease for more than 0.1 Å and Na1-O6 decreases even more (from 2.869(6) to 2.717(9) Å) between 2.0 and 6.6 GPa.

Between 6.56(5) GPa and 7.51(5) GPa, the second phase transition, kernite-II-to-kernite-III, is characterized again by a sharp decrease of the unit-cell volume (Table 1 and Fig. 2); the behavior reflects that expected for a first-order phase transition. Unfortunately, this phase transformation is coupled with a drastic decrease of the number of observed reflections, which ultimately hinders any

structure solution (and refinements) of the kernite-III structure and, therefore, the determination of the nature itself (displacive or reconstructive?) of the second *P*-induced phase transition. We can only infer that this phase transition likely involves the complex H-bonds network, which the bulk volume contraction densifies. Consistently with the study performed by Silva et al. [14], a further possible explanation of this phase transition could be related to a change in the bonding coordination of the BO_3 units.

4.3. Comparison with previous high-pressure data

Although this is the first study that investigates the structure evolution of kernite at increasing pressure *via* X-ray single crystal diffraction technique, kernite has been recently studied by Silva et al. [(14)] by means of *in-situ* infrared and Raman spectroscopies. Therefore, a comparison of the observed behaviors is advisable. Silva et al. [(14)] observed three phase transitions, occurring at about 2.5, 7 and 11 GPa. In response to the first phase transition, the authors observed the loss of a subset of the Na-associated modes and of a sharp OH^- peak [(14)]. The second phase transition was characterized by major variations of the BO_3 vibrational modes, suggesting a change in the bonding coordination of these units. The third phase transition was characterized by the loss of most of the Raman and infrared modes, and interpreted as irreversible upon decompression. The differences between the observed pressures of phase transitions of this study and those reported by Silva et al. [(14)] may be ascribed to the different experimental procedures, and in particular to the choice of the pressure-transmitting medium. Due to the high solubility of kernite in polar solvents, the commonly used alcohol-based *P*-fluid solutions (*e.g.*, methanol:ethanol:H_2O = 16:3:1) cannot be used in this case. In this study, we used Ne as pressure-transmitting fluid, whereas Silva et al. [(14)] used (solid) KBr, which leads to deviation from the hydrostatic compression especially at high pressure [(25)]. The first phase transition reported by Silva et al. [(14)] is consistent with the kernite-I to kernite-II phase transition described in section 4.2 of this study, bracketed between 1.6 and 2.0 GPa. We observed major changes in the Na- coordination environment that are consistent with the interpretations reported by Silva et al. [(14)]. After the second phase transition, which leads to the kernite-III polymorph, the structure solution was hindered by deterioration of the X-ray diffraction pattern (Fig. 1), making difficult a comparison with the data reported in the literature. Silva et al. [(14)] indicated major changes in the BO_3 coordination shell, which indeed can explain the abrupt volume decrease observed (Tab. 1). Such volume contraction leads to a densification of the structure and, therefore, we cannot exclude the occurrence of major changes regarding also the H-bonding network, as suggested by the broadening of the Raman peaks of the O-H stretching region reported by Silva et al. [(14)]. For what concerns the third phase transition suggested by Silva et al. [(14)], we did not detect any substantial

change in the XRD compressional pattern, although the rather unusual behavior of the unit-cell parameters after the kernite-II-to-kernite-III phase transition may suggest the occurrence of a further structural re-arrangement. Data collected in decompression clearly show that, despite a significant hysteresis, the observed phase transition are fully reversible; this can be the result of a static compression experiment performed under hydrostatic conditions in this study, if compared to the irreversible behavior reported by Silva et al. [(14)] under non-hydrostatic conditions.

5. Summary and concluding remarks

In this study, we have investigated, for the first time, the high-pressure behavior of kernite by *in-situ* single crystal X-ray diffraction, up to 14.6 GPa. Data collected at high-pressure show that:

1. Kernite is stable, in its ambient-conditions polymorph, up to 1.6 GPa, which is, however, in excess to the potential pressures at which radiation-shielding materials may be subjected. We expect that the elastic parameters here obtained will be employed for a realistic prediction of the compressional behavior of composite materials in which kernite is used as a filler (*e.g.*, Sorel cements + kernite aggregate; epoxy resins + kernite filler).
2. Between 1.6 and 2.0 GPa, kernite undergoes a first-order phase transition, which is reconstructive in character. The new high-*P* polymorph, kernite-II, has the same space group ($P2_1/c$) of the ambient-pressure-kernite.
3. A dramatic change in the compressional anisotropic scheme is observed between kernite and kernite-II. The most striking effect is the stiffening along the [010] crystallographic direction and the softening along the [100] crystallographic direction, in response to the phase transition.
4. The kernite-to-kernite-II phase transition leads to an increase in the average coordination number of the two crystallographically-independent Na sites (to VII), along with a change of the topological configuration of the polyhedra connections: ribbons of Na-polyhedra connected to form elliptically distorted 10-membered rings.
5. Between 6.5 and 7.5 GPa, a second *P*-induced phase transition occurs, which is a first-order transformation. Unfortunately, a sharp decrease in the number of the observed Bragg reflections prevents the structure solution of the kernite-III polymorph, hindering the description of the structural modifications that drive the phase transition. The nature of the kernite-II-to-kernite-III phase transition (displacive or reconstructive?) remains unknown.
6. The experimental findings of this study resize the *P*-stability field of the ambient-*P* polymorph of kernite, previously determined by *in-situ* IR and Raman experiments (but under non-hydrostatic conditions) [14], as kernite-II is the stable polymorph of kernite (at least) from 2.0

GPa, almost 0.5 GPa less than what previously observed. In addition, no more than two *P*-induced phase transitions have been unambiguously observed at least up to 14.5 GPa, although the occurrence of a further phase transition (as reported by Silva et al. [14]) cannot be ultimately excluded.

The formation of the Na-chains, coupled with the sudden decrease of the unit-cell volume in response to the kernite-to-kernite-II phase transition, likely leads to a densification of the H-bonds network. As seen in other studies (*e.g.*,[10, 26]) the H-bonding networks plays a key role on the bulk compressibility. We cannot exclude that the drastic compression of the structure in response to the second phase transition, reflected by the sudden increase of the linear compressibility along [100], is somehow connected to the collapse of the pervasive H-bonding network, which plays a critical role into the crystalline edifice. Unfortunately, without a structural model of kernite-III, no additional considerations can be offered.

Acknowledgements

We acknowledge DESY (Hamburg, Germany), a member of the Helmholtz Association HGF, for the provision of experimental facilities. Parts of this research were carried out at PETRA III and P02.2. The research leading to this result has been supported by the project CALIPSOplus under the Grant Agreement 730872 from the EU Framework Programme for Research and Innovation HORIZON 2020. DC, GDG, MM, SM, FP, TB and PL acknowledge the support of the Italian Ministry of Education (MIUR) through the project 'Dipartimenti di Eccellenza 2018-2022' and 'PRIN2017 - Mineral reactivity, a key to understand large-scale processes' (2017L83S77). GDG, MM and PL acknowledge the support of the University of Milano through the project “Piano di Sostegno alla Ricerca 2018”. Four anonymous reviewers and the Associate Editor are thanked for their suggestions aimed to improve the quality of the manuscript.

References

1. U.S. Geological Survey. Mineral commodity summaries 2019. Reston, Virginia (USA): 2019
2. Carter RS, Palevsky H, Myers VW, Hughes DJ. Thermal neutron absorption cross sections of boron and gold. Phys Rev. 1953;92(3):716–721.
3. Palmer M, Swihart G. Boron isotope geochemistry: An overview. In: Anovitz L, Grew E, eds. Boron Mineral. Petrol. Geochemistry. Washington: Mineralogical Society of America; 1996:709–744.
4. Gatta GD, Vignola P, Lee Y. Stability of (Cs, K)$Al_4Be_5B_{11}O_{28}$ (londonite) at high pressure and high temperature: a potential neutron absorber material. Phys Chem Miner. 2011;38(6):429–434.
5. Gatta GD, Lotti P, Merlini M, Liermann H-P, Fisch M. High-Pressure Behavior and Phase Stability of Al_5BO_9, a Mullite-Type Ceramic Material. J Am Ceram Soc. 2013;96(8):2583–2592.
6. Lotti P, Gatta GD, Demitri N, Guastella G, Rizzato S, Ortenzi MA et al. Crystal chemistry and temperature behavior of the natural hydrous borate colemanite, a mineral commodity of boron. Phys Chem Miner. 2018;45(5):405–422.
7. Lotti P, Gatta GD, Comboni D, Guastella G, Merlini M, Guastoni A et al. High-pressure behavior and P-induced phase transition of $CaB_3O_4(OH)_3{\cdot}H_2O$ (colemanite). J Am Ceram Soc. 2017;100(5):2209–2220.
8. Hurlbut CS, Aristarain LF, Erd RC. Kernite from Tincalayu, Salta, Argentina. 1973
9. Cooper WF, Larsen FK, Coppens P. Electron Population Analysis Data . V . of Accurate Diffraction Structure and One-Center of the Gharge Refinement Mineral Kernite , $Na_2B_4O_6(OH)_2{\cdot}3H_2O$. Am Mineral. 1973;58:21–31.
10. Gatta GD, Guastoni A, Lotti P, Guastella G, Fabelo O, Fernandez-Diaz MT. A multi-methodological study of kernite, a mineral commodity of boron. Am Mineral. In press 2020.
11. Schaller WT. Borate minerals from the kramer district, mohave desert, california. shorter Contrib to Gen Geol. 1929;137–170.
12. Sennova NA, Bubnova RS, Filatov SK, Paufler P, Meyer DC, Levin AA, et al. Room, low, and high temperature dehydration and phase transitions of kernite in vacuum and in air. Cryst Res Technol. 2005;40(6):563–572.
13. Pabst A, Sawyer DL. Tincalconite Crystals From Searles Lake, San Bernardino County, California. Am Mineral. 1948;33:472–481.
14. Silva M, O' Bannon III EF, Williams Q. A vibrational spectroscopic study of kernite to 25 GPa : Implications for the high-pressure stability of borate polyhedra. Am Mineral.

2018;103(June):1306–1318.

15. Christ CL, Garrels RM. Relations among sodium borate hydrates at the Kramer deposit, Boron, California. Am J Sci. 1959;257(7):516–528.
16. Klotz S, Chervin JC, Munsch P, Le Marchand G. Hydrostatic limits of 11 pressure transmitting media. J Phys D Appl Phys. 2009;42(7).
17. Mao HK, Xu J, Bell PM. Calibration of the ruby pressure gauge to 800 kbar under quasi-hydrostatic conditions. J Geophys Res. 1986;91(B5):4673.
18. Rothkirch A, Gatta GD, Meyer M, Merkel S, Merlini M, Liermann HP. Single-crystal diffraction at the Extreme Conditions beamline P02.2: Procedure for collecting and analyzing high-pressure single-crystal data. J Synchrotron Radiat. 2013;20(5):711–720.
19. Rigaku Oxford Diffraction. CrysAlisPro Software system, version 1.171.38.46. 2018.
20. Petrícek V, Dušek M, Palatinus L. Crystallographic computing system JANA2006: General features. Zeitschrift fur Krist. 2014;229(5):345–352.
21. Palatinus L, Chapuis G. SUPERFLIP - A computer program for the solution of crystal structures by charge flipping in arbitrary dimensions. J Appl Crystallogr. 2007;40(4):786–790.
22. Birch F. Finite elastic strain of cubic crystals. Phys Rev. 1947;71(11):809–824.
23. Angel RJ, Gonzalez-Platas J, Alvaro M. EosFit7c and a Fortran module (library) for equation of state calculations. Zeitschrift fur Krist. 2014;229(5):405–419.
24. Angel RJ. Win_Strain: a program to calculate strain tensors from unit-cell parameters. http://www.rossangel.com/text_strain.htm. Accessed 16 April 2020.
25. Miletich R., Allan DR, Kuhs WF. High-Pressure Single-Crystal Techniques. In Hazen RM, Downs RT, eds. High-temperature and high-pressure crystal chemistry. Mineralogical Society of America; 2000: 445-519.
26. Comboni D, Gatta GD, Lotti P, Merlini M, Hanfland M. Anisotropic compressional behavior of ettringite The high-pressure behavior of a natural ettringite [$Ca_6Al_2(SO_4)_3(OH)_{12}\cdot 27H_2O$. Cem Concr Res. 2019;120:46–51.

Fig.1: Reconstruction, based on the experimental data, of the *h0l** reciprocal lattice plane of kernite-I, -II and -III (from left to right).

Fig.2: Evolution of the unit-cell parameters and unit-cell volume of kernite. Low-pressure polymorph in *black squares*, kernite-II in *red circles* and kernite-III in *upward-blue triangles*. The decompression path is displayed in *downward-green triangles.*

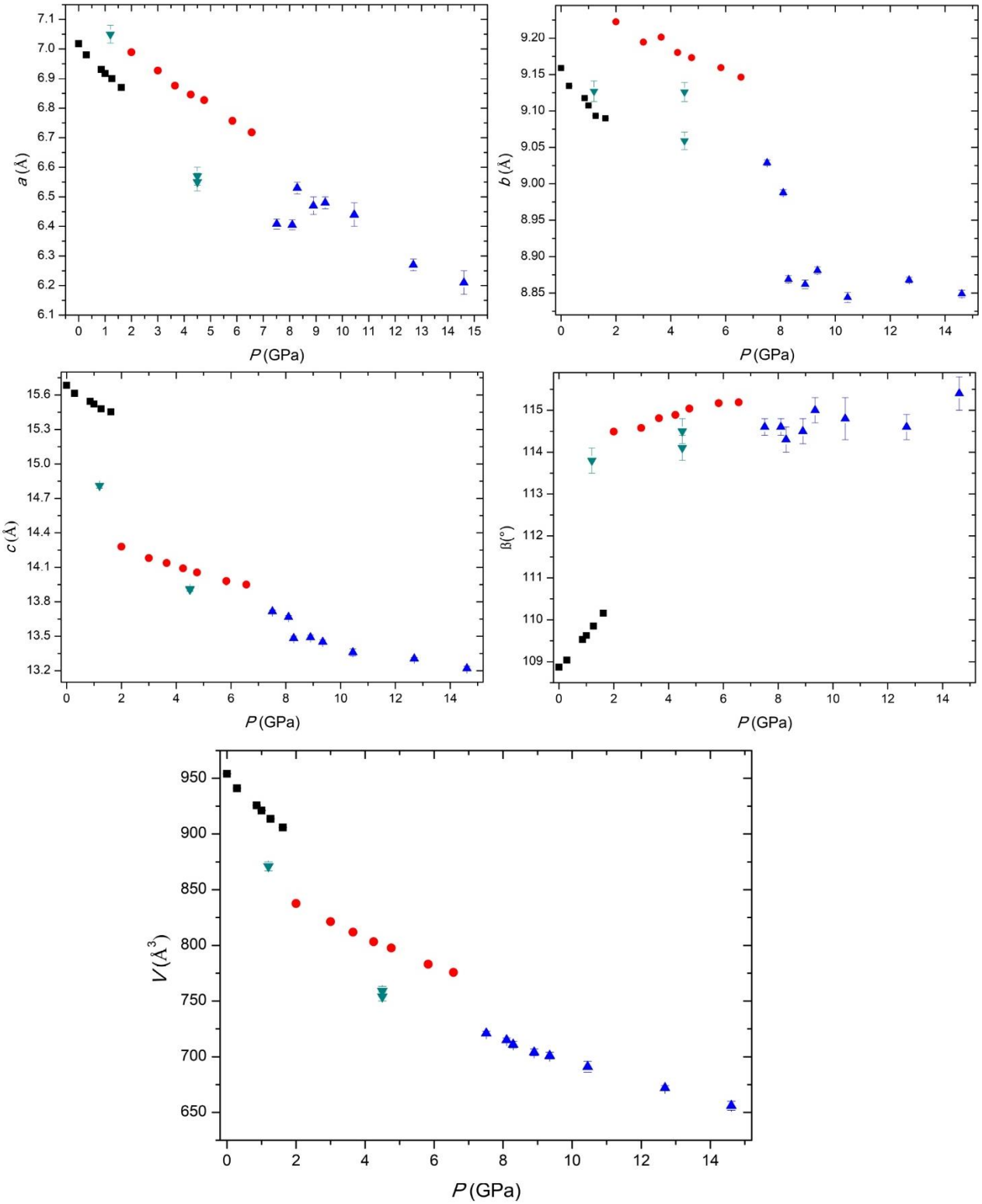

Fig.3: Comparison between the crystal structures of the low- and high- pressure polymorph of kernite (ambient-pressure kernite on the left, kernite-II on the right) viewed down [100] (*top*) and [010] (*bottom*); black arrows indicate the principal deformation mechanisms.

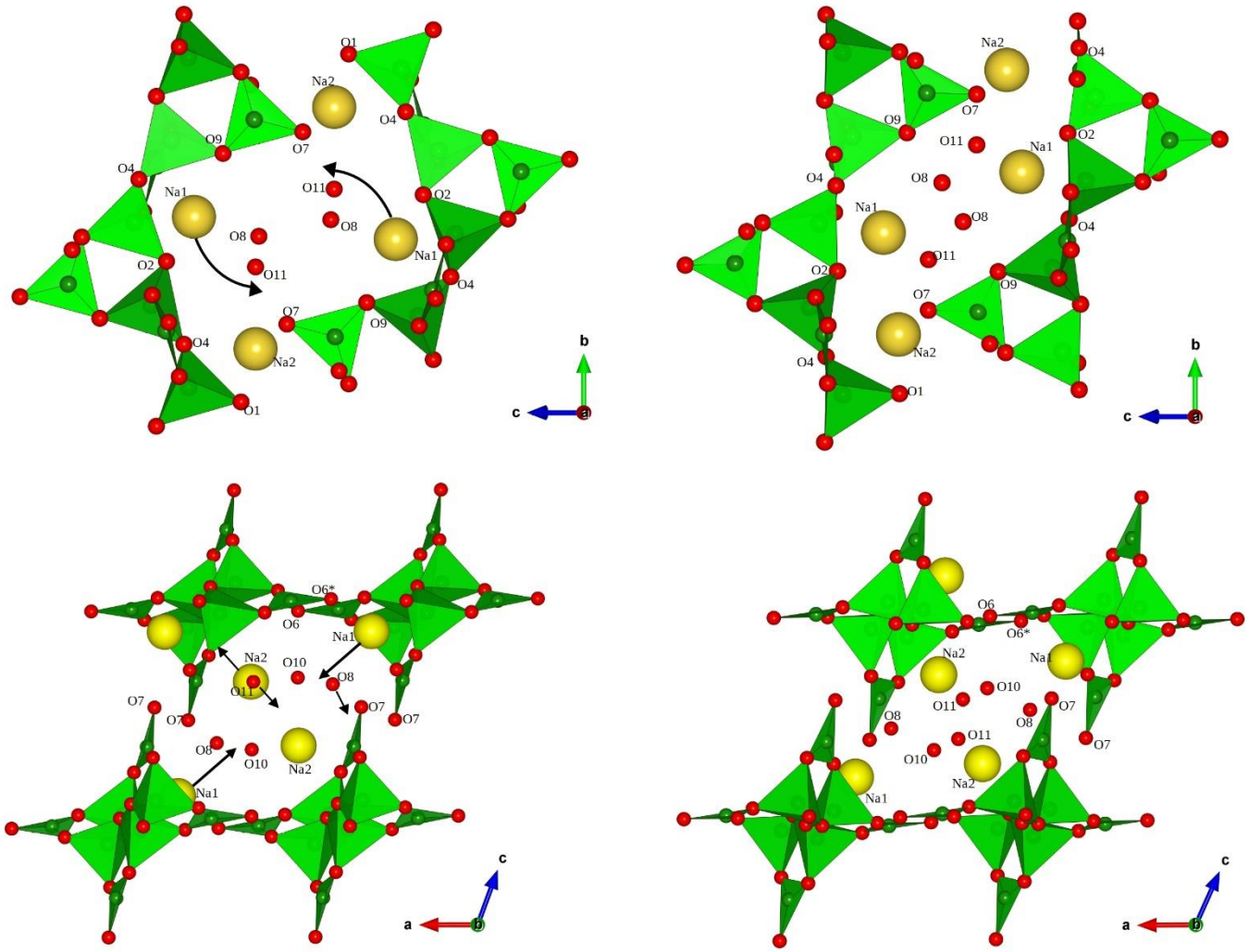

Fig.4: Comparison between Na-polyhedra in the ambient-pressure kernite (*top, left*) and in kernite-II (*top, right*) structure. The phase transition induces the formation of Na-polyhedra ribbons (*bottom, right*) and ultimately complex 10-mRs made by Na-polyhedra.

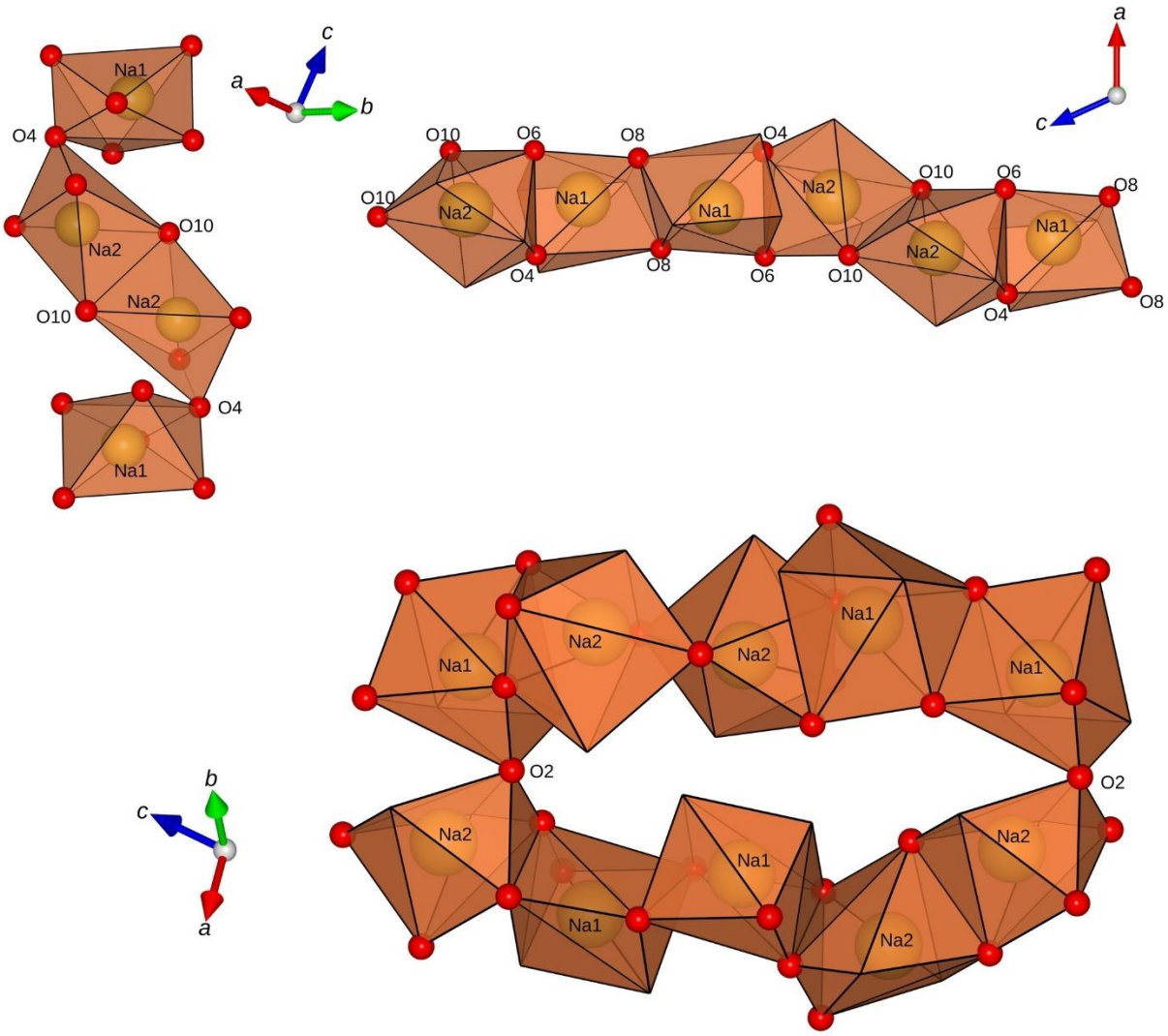

Table 1: Unit-cell parameters of kernite with pressure (* data collected in decompression).

P (GPa)	*V* (Å^3)	*a* (Å)	*b* (Å)	*c* (Å)	*β* (°)
0.0001	954.1(3)	7.018(2)	9.1590(8)	15.685(1)	108.87(2)
0.29(5)	941.0(3)	6.980(2)	9.1344(7)	15.614(1)	109.04(2)
0.86(5)	925.7(2)	6.931(2)	9.1177(5)	15.544(1)	109.53(2)
1.00(5)	921.0(3)	6.917(2)	9.1076(6)	15.522(2)	109.63(2)
1.26(5)	913.6(4)	6.900(3)	9.0934(8)	15.480(2)	109.85(3)
1.62(5)	905.9(2)	6.870(2)	9.0899(5)	15.453(1)	110.16(2)
2.00(5)	837.6(4)	6.989(3)	9.2225(8)	14.280(2)	114.49(3)
3.00(5)	821.3(4)	6.927(3)	9.1946(9)	14.181(2)	114.58(4)
3.65(5)	811.9(5)	6.876(4)	9.201(1)	14.138(3)	114.81(5)
4.25(5)	803.3(4)	6.846(3)	9.1804(9)	14.091(2)	114.89(3)
4.76(5)	797.6(6)	6.827(4)	9.173(1)	14.056(3)	115.04(5)
5.83(5)	783.1(5)	6.757(4)	9.160(1)	13.981(3)	115.17(5)
6.56(5)	775.7(3)	6.718(2)	9.1464(6)	13.950(2)	115.19(3)
7.51(5)	721(2)	6.41(2)	9.029(4)	13.72(1)	114.6(2)
8.10(5)	715(2)	6.41(2)	8.988(4)	13.67(1)	114.6(2)
8.29(5)	711(3)	6.53(2)	8.869(5)	13.48(2)	114.3(3)
8.90(5)	704(3)	6.47(3)	8.862(6)	13.49(2)	114.5(3)
9.35(5)	701(3)	6.48(2)	8.881(5)	13.45(2)	115.0(3)
10.45(5)	691(5)	6.44(4)	8.844(7)	13.36(3)	114.8(5)
12.69(5)	672(2)	6.27(2)	8.868(4)	13.31(1)	114.6(3)
14.61(5)	656(4)	6.21(4)	8.849(5)	13.22(2)	115.4(4)
4.50(5)*	754(4)	6.57(3)	9.06(1)	13.91(2)	114.5(3)
4.50(5)*	759(4)	6.55(3)	9.13(1)	13.91(2)	114.1(3)
1.20(5)*	871(4)	7.05(3)	9.13(1)	14.81(2)	113.8(3)

Table 2: Relevant O-O-O angles (in °) based on the structure refinements at high pressure (see text for details).

P (GPa)	O2-O4-O9 (°)	O1-O4-O2 (°)
0.0001	89.66(8)	146.6(1)
0.29(5)	89.5(1)	146.6(1)
0.86(5)	89.2(1)	146.9(2)
1.00(5)	89.3(1)	146.8(1)
1.26(5)	89.4(1)	146.9(2)
1.62(5)	89.3(1)	147.0(2)
2.00(5)	124.5(2)	111.8(2)
3.00(5)	123.9(2)	112.0(2)
3.65(5)	124.0(2)	112.1(2)
4.25(5)	123.8(2)	112.2(2)
4.76(5)	123.5(2)	112.3(2)
5.83(5)	123.7(2)	111.9(2)
6.56(5)	124.5(2)	110.5(3)

Table 3: Na-O distances (in Å) based on the structure refinements at high pressure.

P (GPa)	Na2-O4	Na2-O1	Na2-O10	Na2-O10	Na2-O11	Na2-O6	Na2-O2
0.0001	2.400(3)	2.483(4)	2.442(3)	2.435(4)	2.294(3)	3.114(4)	3.627(2)
0.29(5)	2.388(4)	2.497(5)	2.418(3)	2.431(5)	2.281(3)	3.071(6)	3.607(3)
0.86(5)	2.362(4)	2.503(5)	2.389(4)	2.416(6)	2.276(3)	3.013(6)	3.579(3)
1.00(5)	2.363(4)	2.509(5)	2.386(3)	2.411(5)	2.275(3)	2.995(5)	3.568(3)
1.26(5)	2.352(4)	2.515(5)	2.366(3)	2.409(5)	2.267(3)	2.962(6)	3.552(3)
1.62(5)	2.343(5)	2.532(7)	2.347(5)	2.399(7)	2.261(4)	2.930(8)	3.545(4)
2.00(5)	2.385(5)	2.706(7)	2.463(4)	2.453(6)	2.463(4)	2.533(8)	2.509(4)
3.00(5)	2.375(6)	2.700(8)	2.425(4)	2.446(7)	2.424(5)	2.497(9)	2.494(4)
3.65(5)	2.366(5)	2.696(7)	2.401(4)	2.439(6)	2.401(4)	2.477(8)	2.494(4)
4.25(5)	2.362(5)	2.698(7)	2.381(4)	2.429(6)	2.381(4)	2.457(8)	2.490(4)
4.76(5)	2.347(5)	2.690(7)	2.369(4)	2.432(6)	2.369(4)	2.447(8)	2.479(4)
5.83(5)	2.343(5)	2.674(7)	2.337(4)	2.419(6)	2.337(4)	2.426(7)	2.467(4)
6.56(5)	2.377(7)	2.67(1)	2.332(6)	2.392(8)	2.332(6)	2.42(1)	2.462(5)

P (GPa)	Na1-O4	Na1-O2	Na1-O3	Na1-O9	Na1-O6*	Na1-O6	Na1-O7	Na1-O8	Na1-O8
0.0001	2.396(3)	2.432(4)	2.511(2)	2.413(3)	2.399(4)	3.909(4)	4.025(2)	4.258(3)	2.303(4)
0.29(5)	2.386(4)	2.425(5)	2.497(3)	2.409(4)	2.389(5)	3.894(5)	3.998(3)	4.229(5)	2.289(5)
0.86(5)	2.381(5)	2.419(5)	2.475(3)	2.407(4)	2.370(5)	3.886(6)	3.965(3)	4.142(6)	2.274(6)
1.00(5)	2.376(4)	2.419(5)	2.471(3)	2.403(4)	2.374(5)	3.877(5)	3.953(3)	4.163(5)	2.272(5)
1.26(5)	2.372(4)	2.416(5)	2.462(3)	2.401(4)	2.367(5)	3.873(6)	3.931(3)	4.135(5)	2.261(6)
1.62(5)	2.369(6)	2.407(7)	2.448(4)	2.410(6)	2.376(7)	3.858(8)	3.909(4)	4.099(6)	2.254(8)
2.00(5)	2.309(5)	2.592(7)	2.524(4)	3.177(5)	2.869(6)	3.795(8)	2.460(4)	2.373(8)	2.528(7)
3.00(5)	2.294(5)	2.588(8)	2.526(4)	3.144(5)	2.838(7)	3.779(7)	2.433(5)	2.360(9)	2.529(8)
3.65(5)	2.297(5)	2.575(7)	2.520(4)	3.128(5)	2.827(6)	3.763(7)	2.429(4)	2.361(8)	2.526(7)
4.25(5)	2.298(5)	2.571(7)	2.519(4)	3.113(5)	2.812(6)	3.745(7)	2.417(4)	2.353(7)	2.518(7)
4.76(5)	2.299(5)	2.574(7)	2.517(4)	3.100(5)	2.800(6)	3.731(7)	2.406(4)	2.35(07)	2.515(7)
5.83(5)	2.292(4)	2.568(7)	2.515(4)	3.085(5)	2.764(5)	3.692(7)	2.393(4)	2.342(7)	2.536(6)
6.56(5)	2.287(7)	2.56(1)	2.465(6)	3.141(8)	2.717(9)	3.592(11)	2.375(6)	2.34(1)	2.63(1)

Table 4: Refined elastic parameters pertaining to the different polymorphs of kernite based on the isothermal II-BM Equation of State fits (*fixed parameter, ** along *b*, the structure is substantially uncompressible after the second phase transition, see also Table 1 and Fig. 2).

	V_0, x_0 (Å^3, Å)	$K_{V0,\,x0}$ (GPa)	K'	$\beta_{V0,\,x0}$ (GPa^{-1})
V	952(1)	29(1)	4*	0.035(1)
a	7.013(4)	23(1)	4*	0.0147(6)
b	9.154(5)	66(7)	4*	0.0051(6)
c	15.67(1)	33(2)	4*	0.0101(8)
				II-BM EoS, *P*< 1.60(5) GPa
Kernite-II	V_0, x_0 (Å^3, Å)	$K_{V0,\,x0}$ (GPa)	K'	$\beta_{V0,\,x0}$ (GPa^{-1})
V	873(1)	43.3(9)	4*	0.023(5)
a	7.17(1)	22(1)	4*	0.0147(6)
b	9.253(6)	175(13)	4*	0.0019(2)
c	14.45(1)	49(2)	4*	0.0068(3)
				II-BM EoS, 2.00(5)<*P*< 6.56(5) GPa
Kernite-III	V_0, x_0 (Å^3, Å)	$K_{V0,\,x0}$ (GPa)	K'	$\beta_{V0,\,x0}$ (GPa^{-1})
V	839(10)	36(3)	4*	0.028(2)
a	8.0(4)	4(2)	4*	0.09(4)
b	**	**	**	**
c	14.8(2)	21(6)	4*	0.016(4)
				II-BM EoS, 7.51(5)<*P*< 14.61 (5) GPa

Table S1: Refined anisotropic atomic displacement parameters (Å^2) of kernite as a function of pressure.

	P(GPa)	U_{11}	U_{22}	U_{33}	U_{12}	U_{13}	U_{23}
Na1	0.0001	0.021(2)	0.0222(7)	0.031(5)	-0.0010(5)	0.0206(8)	-0.0009(4)
	0.29(5)	0.024(3)	0.0213(8)	0.0303(7)	-0.0007(6)	0.022(1)	-0.0001(5)
	0.86(5)	0.028(3)	0.020(1)	0.030(1)	-0.001(1)	0.022(1)	0.000(1)
	1.00(5)	0.026(3)	0.0207(8)	0.0291(7)	-0.0008(6)	0.020(1)	-0.0001(5)
	1.26(5)	0.032(3)	0.0178(8)	0.0337(8)	-0.0009(7)	0.028(1)	-0.0001(6)
	1.62(5)	0.035(4)	0.017(1)	0.032(1)	-0.0008(9)	0.028(2)	0.0005(8)
	2.00(5)	0.069(6)	0.036(1)	0.044(1)	-0.001(1)	0.045(2)	0.0008(1)
	3.00(5)	0.074(5)	0.033(1)	0.043(1)	0.000(1)	0.044(2)	0.0010(9)
	3.65(5)	0.0475(9)	0.036(1)	0.042(1)	0.001(1)	0.038(1)	0.0003(9)
	4.25(5)	0.062(6)	0.031(1)	0.041(1)	0.001(1)	0.040(2)	0.0017(9)
	4.76(5)	0.070(6)	0.031(1)	0.045(1)	0.002(1)	0.047(2)	0.0024(9)
	5.83(5)	0.070(5)	0.029(1)	0.046(1)	0.003(1)	0.047(2)	0.0032(9)
	6.56(5)	0.085(9)	0.038(2)	0.066(2)	0.012(2)	0.070(4)	0.011(2)
Na2	0.0001	0.021(2)	0.0290(8)	0.0371(6)	-0.0019(6)	0.0009(9)	0.0008(5)
	0.29(5)	0.029(4)	0.028(1)	0.038(1)	-0.001(1)	0.007(1)	0.001(1)
	0.86(5)	0.026(4)	0.029(1)	0.0342(8)	-0.0013(8)	0.003(1)	0.0009(7)
	1.00(5)	0.036(3)	0.0256(9)	0.0336(7)	0.0000(8)	0.003(1)	0.0016(6)
	1.26(5)	0.027(4)	0.025(1)	0.0343(8)	0.0005(8)	0.002(1)	0.0014(7)
	1.62(5)	0.034(5)	0.024(1)	0.033(1)	0.001(1)	0.006(2)	0.001(1)
	2.00(5)	0.027(4)	0.027(1)	0.0268(9)	0.0011(9)	0.010(2)	-0.0003(8)
	3.00(5)	0.032(4)	0.025(1)	0.0247(8)	0.0002(9)	0.012(1)	-0.0007(7)
	3.65(5)	0.038(4)	0.024(1)	0.0256(9)	0.0012(9)	0.015(2)	-0.0007(7)
	4.25(5)	0.031(4)	0.023(1)	0.0223(8)	0.0003(9)	0.012(2)	-0.0007(7)
	4.76(5)	0.03(4)	0.025(1)	0.0235(8)	-0.0001(9)	0.013(2)	-0.0015(7)
	5.83(5)	0.032(4)	0.023(1)	0.0223(8)	0.0010(9)	0.013(1)	-0.0005(7)
	6.56(5)	0.013(6)	0.035(2)	0.028(1)	-0.002(1)	0.013(2)	-0.002(1)
O1	0.0001	0.029(3)	0.0129(9)	0.0148(6)	0.0025(7)	0.013(1)	0.0011(5)
	0.29(5)	0.026(4)	0.014(1)	0.016(1)	0.002(1)	0.014(1)	0.001(1)
	0.86(5)	0.032(4)	0.012(1)	0.0145(8)	0.002(1)	0.014(2)	0.0013(8)
	1.00(5)	0.027(4)	0.013(1)	0.0134(7)	0.0035(9)	0.010(1)	0.0012(7)
	1.26(5)	0.029(5)	0.012(1)	0.0147(8)	0.002(1)	0.013(1)	0.0006(8)
	1.62(5)	0.036(6)	0.009(2)	0.013(1)	0.002(1)	0.015(2)	0.001(1)
O2	0.0001	0.014(3)	0.0122(9)	0.0151(6)	-0.0023(7)	0.008(1)	0.0003(6)
	0.29(5)	0.014(4)	0.013(1)	0.016(1)	-0.003(1)	0.011(1)	0.000(1)
	0.86(5)	0.017(4)	0.013(1)	0.0157(8)	-0.0041(9)	0.011(1)	0.0007(8)
	1.00(5)	0.010(4)	0.014(1)	0.0145(7)	-0.0033(8)	0.008(1)	0.0004(7)
	1.26(5)	0.015(4)	0.012(1)	0.0159(8)	-0.0021(9)	0.011(1)	0.0023(7)
	1.62(5)	0.024(6)	0.009(1)	0.016(1)	-0.003(1)	0.013(2)	0.001(1)
O5	0.0001	0.010(3)	0.017(1)	0.0319(9)	-0.0002(7)	0.015(1)	0.0018(7)
	0.29(5)	0.014(4)	0.015(1)	0.032(1)	0.002(1)	0.017(2)	0.004(1)
	0.86(5)	0.021(5)	0.014(1)	0.030(1)	0.003(1)	0.017(2)	0.005(1)
	1.00(5)	0.012(4)	0.016(1)	0.029(1)	0.0013(9)	0.013(2)	0.0034(8)
	1.26(5)	0.018(5)	0.013(1)	0.032(1)	0.0023(9)	0.017(2)	0.0050(9)
	1.62(5)	0.005(6)	0.017(2)	0.029(2)	0.001(1)	0.013(3)	0.005(1)

	P(GPa)	U_{11}	U_{22}	U_{33}	U_{12}	U_{13}	U_{23}
O7	0.0001	0.059(4)	0.021(1)	0.0168(7)	0.010(1)	0.020(1)	0.0041(7)
	0.29(5)	0.057(5)	0.022(1)	0.018(1)	0.009(1)	0.021(2)	0.004(1)
	0.86(5)	0.062(6)	0.020(1)	0.016(1)	0.010(1)	0.020(2)	0.005(1)
	1.00(5)	0.071(5)	0.021(1)	0.0161(8)	0.012(1)	0.021(2)	0.0044(8)
	1.26(5)	0.064(6)	0.019(1)	0.0173(9)	0.012(1)	0.022(2)	0.006(9)
	1.62(5)	0.069(8)	0.019(2)	0.017(1)	0.011(2)	0.027(3)	0.004(1)
O8	0.0001	0.041(5)	0.036(1)	0.032(1)	0.008(1)	0.025(1)	0.007(1)
	0.29(5)	0.050(7)	0.037(2)	0.033(1)	0.010(2)	0.029(2)	0.008(1)
	0.86(5)	0.048(7)	0.035(2)	0.031(1)	0.007(2)	0.026(3)	0.004(1)
	1.00(5)	0.047(6)	0.033(2)	0.030(1)	0.007(1)	0.024(2)	0.006(1)
	1.26(5)	0.046(7)	0.032(2)	0.032(1)	0.009(2)	0.025(2)	0.007(1)
	1.62(5)	0.047(1)	0.033(3)	0.030(2)	0.010(2)	0.027(3)	0.007(2)
O9	0.0001	0.027(3)	0.0136(9)	0.0153(6)	0.0026(7)	0.013(1)	0.0006(6)
	0.29(5)	0.021(4)	0.014(1)	0.016(1)	0.004(1)	0.014(1)	0.002(1)
	0.86(5)	0.027(4)	0.014(1)	0.0154(8)	0.005(1)	0.014(2)	0.0015(8)
	1.00(5)	0.018(4)	0.015(1)	0.0144(7)	0.0048(9)	0.009(1)	0.0023(7)
	1.26(5)	0.023(4)	0.014(1)	0.0169(8)	0.005(1)	0.015(2)	0.0035(8)
	1.62(5)	0.023(6)	0.013(2)	0.014(1)	0.005(1)	0.012(2)	0.003(1)
O10	0.0001	0.017(5)	0.041(2)	0.0272(9)	-0.008(1)	0.012(2)	-0.0047(9)
	0.29(5)	0.016(6)	0.041(2)	0.027(1)	-0.008(1)	0.013(2)	-0.004(1)
	0.86(5)	0.024(6)	0.037(2)	0.024(1)	-0.009(2)	0.012(2)	-0.004(1)
	1.00(5)	0.031(6)	0.036(2)	0.025(1)	-0.006(1)	0.015(2)	-0.004(1)
	1.26(5)	0.014(6)	0.037(2)	0.024(1)	-0.006(1)	0.010(2)	-0.004(1)
	1.62(5)	0.028(9)	0.034(3)	0.022(1)	-0.006(2)	0.015(3)	-0.005(2)
O11	0.0001	0.026(4)	0.031(1)	0.0256(8)	0.000(1)	0.009(1)	-0.0021(8)
	0.29(5)	0.033(6)	0.031(2)	0.027(1)	-0.001(1)	0.014(2)	-0.003(1)
	0.86(5)	0.031(6)	0.029(2)	0.023(1)	-0.001(1)	0.008(2)	-0.003(1)
	1.00(5)	0.026(5)	0.030(2)	0.023(1)	0.002(1)	0.007(2)	-0.002(1)
	1.26(5)	0.033(6)	0.026(2)	0.023(1)	0.000(1)	0.008(2)	-0.003(1)
	1.62(5)	0.035(8)	0.024(2)	0.021(1)	0.001(2)	0.008(3)	-0.002(1)

Table S1: Fractional atomic coordinates and atomic isotropic or equivalent displacement parameters (Å^2) of kernite as a function of pressure.

Site	*P*(GPa)	*s.o.f*	*x*	*y*	*z*	*Uiso*(Å^2)
Na1	0.0001	1	0.3196(3)	0.4647(1)	0.31092(8)	0.022(1)
	0.29(5)	1	0.3195(4)	0.4646(1)	0.3108(1)	0.022(1)
	0.86(5)	1	0.3204(5)	0.4653(2)	0.3107(1)	0.023(1)
	1.00(5)	1	0.3209(4)	0.4651(1)	0.3107(1)	0.022(1)
	1.26(5)	1	0.3211(5)	0.4651(2)	0.3107(1)	0.024(1)
	1.62(5)	1	0.3224(7)	0.4658(2)	0.3108(2)	0.023(2)
	2.00(5)	1	0.3681(7)	0.4112(2)	0.3577(2)	0.042(3)
	3.00(5)	1	0.3674(7)	0.4119(2)	0.3577(2)	0.043(2)
	3.65(5)	1	0.3671(7)	0.4121(2)	0.3574(2)	0.0356(8)
	4.25(5)	1	0.3659(8)	0.4126(2)	0.3571(2)	0.038(2)
	4.76(5)	1	0.3645(8)	0.4125(2)	0.3568(2)	0.041(3)
	5.83(5)	1	0.3603(7)	0.4124(2)	0.3553(2)	0.040(2)
	6.56(5)	1	0.3460(4)	0.4085(1)	0.3494(1)	0.050(1)
Na2	0.0001	1	0.1845(4)	0.3665(1)	0.0723(1)	0.031(1)
	0.29(5)	1	0.1825(5)	0.3668(2)	0.0725(1)	0.033(1)
	0.86(5)	1	0.1782(5)	0.3665(2)	0.0730(1)	0.031(1)
	1.00(5)	1	0.1774(5)	0.3662(2)	0.0731(1)	0.034(1)
	1.26(5)	1	0.1760(5)	0.3666(2)	0.0735(1)	0.031(1)
	1.62(5)	1	0.1717(7)	0.3869(3)	0.0735(2)	0.032(2)
	2.00(5)	1	0.1937(6)	0.6131(2)	0.1114(2)	0.027(2)
	3.00(5)	1	0.1914(6)	0.6134(2)	0.1103(1)	0.027(2)
	3.65(5)	1	0.1896(6)	0.6136(2)	0.1096(2)	0.028(2)
	4.25(5)	1	0.1879(6)	0.6136(2)	0.1089(1)	0.025(2)
	4.76(5)	1	0.1882(6)	0.6136(2)	0.1088(2)	0.025(2)
	5.83(5)	1	0.1866(6)	0.6137(2)	0.1079(1)	0.025(2)
	6.56(5)	1	0.1853(5)	0.6128(2)	0.1064(1)	0.024(1)
B1	0.0001	1	0.4474(8)	0.6678(3)	0.0785(2)	0.0159(5)
	0.29(5)	1	0.447(1)	0.6681(4)	0.0784(2)	0.015(1)
	0.86(5)	1	0.444(1)	0.6692(4)	0.0771(2)	0.0152(7)
	1.00(5)	1	0.442(1)	0.6697(4)	0.0766(2)	0.0155(6)
	1.26(5)	1	0.442(1)	0.6699(4)	0.0761(2)	0.0149(7)
	1.62(5)	1	0.441(1)	0.6707(5)	0.0759(3)	0.0134(9)
	2.00(5)	1	0.422(1)	0.3199(4)	0.0530(3)	0.0139(8)
	3.00(5)	1	0.421(1)	0.3190(5)	0.0517(4)	0.0206(9)
	3.65(5)	1	0.420(1)	0.3183(4)	0.0506(3)	0.0134(7)
	4.25(5)	1	0.422(1)	0.3185(4)	0.0505(3)	0.0134(7)
	4.76(5)	1	0.422(1)	0.3185(4)	0.0499(3)	0.0139(8)
	5.83(5)	1	0.422(1)	0.3178(4)	0.0486(3)	0.0138(7)
	6.56(5)	1	0.426(1)	0.3173(4)	0.0487(2)	0.020(1)

Site	*P*(GPa)	*s.o.f*	*x*	*y*	*z*	*Uiso*(Å^2)
B2	0.0001	1	0.5528(8)	0.2328(3)	0.2686(2)	0.0142(5)
	0.29(5)	1	0.552(1)	0.2334(3)	0.2686(2)	0.015(1)
	0.86(5)	1	0.554(1)	0.2340(4)	0.2689(2)	0.013(1)
	1.00(5)	1	0.555(1)	0.2338(3)	0.2689(2)	0.0135(6)
	1.26(5)	1	0.556(1)	0.2337(4)	0.2693(2)	0.0133(6)
	1.62(5)	1	0.556(1)	0.2340(5)	0.2690(3)	0.0121(8)
	2.00(5)	1	0.581(1)	0.6923(4)	0.2941(3)	0.0124(7)
	3.00(5)	1	0.580(1)	0.6916(4)	0.2937(3)	0.013(7)
	3.65(5)	1	0.578(1)	0.6923(4)	0.2941(3)	0.0125(7)
	4.25(5)	1	0.579(1)	0.6915(4)	0.2942(3)	0.0123(7)
	4.76(5)	1	0.578(1)	0.6916(4)	0.2942(3)	0.0128(7)
	5.83(5)	1	0.579(1)	0.6903(4)	0.2950(3)	0.0132(7)
	6.56(5)	1	0.583(1)	0.6881(3)	0.2971(2)	0.019(1)
B3	0.0001	1	0.574(7)	0.4799(3)	0.1998(2)	0.0124(5)
	0.29(5)	1	0.575(1)	0.4806(3)	0.1994(2)	0.013(1)
	0.86(5)	1	0.576(1)	0.4813(4)	0.1992(2)	0.0139(7)
	1.00(5)	1	0.577(1)	0.4815(3)	0.1993(2)	0.0126(6)
	1.26(5)	1	0.576(1)	0.4811(4)	0.1989(2)	0.0135(6)
	1.62(5)	1	0.576(1)	0.4827(5)	0.1991(3)	0.0119(8)
	2.00(5)	1	0.601(1)	0.4372(4)	0.2261(3)	0.0119(7)
	3.00(5)	1	0.602(1)	0.4370(4)	0.2262(3)	0.0122(7)
	3.65(5)	1	0.602(1)	0.4373(4)	0.2261(3)	0.0119(7)
	4.25(5)	1	0.602(1)	0.4370(4)	0.2257(3)	0.0114(7)
	4.76(5)	1	0.601(1)	0.4369(4)	0.2253(3)	0.012(7)
	5.83(5)	1	0.603(1)	0.4364(4)	0.2260(3)	0.0115(7)
	6.56(5)	1	0.608(1)	0.4338(3)	0.2269(2)	0.016(1)
B4	0.0001	1	0.1313(9)	0.8142(3)	0.2580(2)	0.0212(6)
	0.29(5)	1	0.129(1)	0.8137(4)	0.2580(3)	0.020(1)
	0.86(5)	1	0.127(1)	0.8139(5)	0.2590(3)	0.0211(8)
	1.00(5)	1	0.125(1)	0.8135(4)	0.2587(3)	0.0213(7)
	1.26(5)	1	0.125(1)	0.8136(4)	0.2590(3)	0.0198(8)
	1.62(5)	1	0.123(2)	0.8125(6)	0.2587(4)	0.020(1)
	2.00(5)	1	0.112(2)	0.1135(5)	0.2357(4)	0.021(1)
	3.00(5)	1	0.109(1)	0.114854)	0.2356(4)	0.0141(7)
	3.65(5)	1	0.108(2)	0.1149(5)	0.2350(4)	0.0203(9)
	4.25(5)	1	0.107(2)	0.1150(5)	0.2345(4)	0.0199(9)
	4.76(5)	1	0.105(2)	0.1151(5)	0.2348(4)	0.0185(9)
	5.83(5)	1	0.102(1)	0.1151(5)	0.2338(4)	0.0187(8)
	6.56(5)	1	0.086(1)	0.1114(4)	0.2285(3)	0.025(1)

Site	*P*(GPa)	*s.o.f*	*x*	*y*	*z*	*Uiso*(Å^2)
O1	0.0001	1	0.4862(5)	0.5252(2)	0.1026(1)	0.018(1)
	0.29(5)	1	0.4881(7)	0.5258(2)	0.1024(1)	0.017(2)
	0.86(5)	1	0.4875(7)	0.5261(2)	0.1017(2)	0.018(2)
	1.00(5)	1	0.4876(6)	0.5267(2)	0.1015(1)	0.017(2)
	1.26(5)	1	0.4876(7)	0.5269(2)	0.1013(2)	0.017(2)
	1.62(5)	1	0.488(1)	0.5273(3)	0.1008(2)	0.018(2)
	2.00(5)	1	0.5044(9)	0.4399(3)	0.1092(2)	0.0183(6)
	3.00(5)	1	0.5037(9)	0.4397(3)	0.1084(2)	0.0184(6)
	3.65(5)	1	0.5038(9)	0.4396(3)	0.1080(2)	0.0178(6)
	4.25(5)	1	0.5045(9)	0.4395(3)	0.1078(2)	0.0173(6)
	4.76(5)	1	0.504(1)	0.4395(3)	0.1076(2)	0.0191(6)
	5.83(5)	1	0.5033(9)	0.4395(3)	0.1067(2)	0.0195(6)
	6.56(5)	1	0.5030(7)	0.4370(2)	0.1068(1)	0.023(2)
O2	0.0001	1	0.5600(5)	0.5992(2)	0.2590(1)	0.013(1)
	0.29(5)	1	0.5603(6)	0.5994(2)	0.2591(1)	0.013(2)
	0.86(5)	1	0.5619(7)	0.6002(2)	0.2592(2)	0.014(2)
	1.00(5)	1	0.5628(6)	0.6003(2)	0.2593(1)	0.012(1)
	1.26(5)	1	0.5628(7)	0.6007(2)	0.2593(2)	0.013(2)
	1.62(5)	1	0.5636(9)	0.6010(3)	0.2594(2)	0.015(2)
	2.00(5)	1	0.4213(8)	0.7983(3)	0.2369(2)	0.013(5)
	3.00(5)	1	0.4194(8)	0.7980(3)	0.2363(2)	0.013(5)
	3.65(5)	1	0.4198(8)	0.7982(3)	0.2363(2)	0.013(5)
	4.25(5)	1	0.4200(8)	0.7978(3)	0.2362(2)	0.012(5)
	4.76(5)	1	0.4187(8)	0.7979(3)	0.2359(2)	0.013(5)
	5.83(5)	1	0.4176(8)	0.7976(3)	0.2355(2)	0.012(6)
	6.56(5)	1	0.4180(6)	0.7956(2)	0.2349(1)	0.017(2)
O3	0.0001	1	0.2330(5)	0.7059(2)	0.2317(1)	0.0205(4)
	0.29(5)	1	0.2312(7)	0.7052(3)	0.2318(2)	0.020(1)
	0.86(5)	1	0.2303(8)	0.7047(3)	0.2324(2)	0.0200(6)
	1.00(5)	1	0.2298(7)	0.7042(3)	0.2324(2)	0.0195(5)
	1.26(5)	1	0.2287(8)	0.7040(3)	0.2327(2)	0.0191(5)
	1.62(5)	1	0.228(1)	0.7032(4)	0.2329(2)	0.0184(7)
	2.00(5)	1	0.7790(9)	0.7215(3)	0.2815(2)	0.019(6)
	3.00(5)	1	0.7819(9)	0.7220(3)	0.2830(2)	0.0186(6)
	3.65(5)	1	0.7817(9)	0.7224(3)	0.2835(2)	0.0179(6)
	4.25(5)	1	0.7830(9)	0.7226(3)	0.2844(2)	0.018(6)
	4.76(5)	1	0.7841(9)	0.7222(3)	0.2850(2)	0.0193(6)
	5.83(5)	1	0.7869(9)	0.7213(3)	0.2868(2)	0.0187(6)
	6.56(5)	1	0.7920(7)	0.7192(3)	0.2893(2)	0.025(1)

Site	*P*(GPa)	*s.o.f*	*x*	*y*	*z*	*Uiso*(Å^2)
O4	0.0001	1	0.4649(5)	0.3511(2)	0.2090(1)	0.0137(3)
	0.29(5)	1	0.4649(6)	0.3511(2)	0.2089(1)	0.0139(4)
	0.86(5)	1	0.4642(7)	0.3517(2)	0.2082(2)	0.0140(5)
	1.00(5)	1	0.4653(6)	0.3521(2)	0.2084(1)	0.0134(4)
	1.26(5)	1	0.4653(6)	0.3525(2)	0.2083(1)	0.0130(4)
	1.62(5)	1	0.4643(9)	0.3523(3)	0.2079(2)	0.0122(6)
	2.00(5)	1	0.5004(9)	0.5486(3)	0.2602(2)	0.0175(6)
	3.00(5)	1	0.4990(8)	0.5487(3)	0.2596(2)	0.0178(6)
	3.65(5)	1	0.4993(9)	0.5485(3)	0.2595(2)	0.0179(6)
	4.25(5)	1	0.4988(9)	0.5482(3)	0.2591(2)	0.0174(6)
	4.76(5)	1	0.4980(9)	0.5485(3)	0.2590(2)	0.0174(6)
	5.83(5)	1	0.4983(9)	0.5479(3)	0.2594(2)	0.0183(6)
	6.56(5)	1	0.5000(6)	0.5436(2)	0.2614(1)	0.024(4)
O5	0.0001	1	0.790(5)	0.4485(2)	0.2152(1)	0.018(1)
	0.29(5)	1	0.793(7)	0.4489(2)	0.2158(2)	0.018(2)
	0.86(5)	1	0.794(1)	0.4495(3)	0.2160(2)	0.020(2)
	1.00(5)	1	0.796(7)	0.4495(2)	0.2163(2)	0.017(2)
	1.26(5)	1	0.796(7)	0.4495(2)	0.2162(2)	0.019(2)
	1.62(5)	1	0.797(1)	0.4505(4)	0.2165(3)	0.015(3)
	2.00(5)	1	0.829(1)	0.4702(3)	0.2571(2)	0.0237(7)
	3.00(5)	1	0.8314(9)	0.4708(3)	0.2574(2)	0.0234(7)
	3.65(5)	1	0.833(1)	0.4709(3)	0.2573(3)	0.0227(7)
	4.25(5)	1	0.834(1)	0.4709(3)	0.2576(3)	0.0221(7)
	4.76(5)	1	0.836(1)	0.4712(3)	0.2577(3)	0.0219(7)
	5.83(5)	1	0.837(1)	0.4708(3)	0.2576(2)	0.0214(6)
	6.56(5)	1	0.8400(7)	0.4666(2)	0.2591(2)	0.027(2)
O6	0.0001	1	0.0621(7)	0.2897(3)	0.2408(2)	0.0355(6)
	0.29(5)	1	0.0635(9)	0.2888(3)	0.2398(2)	0.034(1)
	0.86(5)	1	0.068(1)	0.2875(4)	0.2391(2)	0.0344(8)
	1.00(5)	1	0.0676(9)	0.2872(3)	0.2382(2)	0.0341(7)
	1.26(5)	1	0.069(1)	0.2869(3)	0.2374(2)	0.0346(8)
	1.62(5)	1	0.069(1)	0.2862(5)	0.2363(3)	0.032(1)
	2.00(5)	1	0.077(1)	0.6396(4)	0.2564(3)	0.038(1)
	3.00(5)	1	0.081(1)	0.6407(4)	0.2558(3)	0.0362(9)
	3.65(5)	1	0.082(1)	0.6410(4)	0.2552(3)	0.035(1)
	4.25(5)	1	0.083(1)	0.6417(4)	0.2545(3)	0.0327(9)
	4.76(5)	1	0.083(1)	0.6417(4)	0.2542(3)	0.0328(9)
	5.83(5)	1	0.086(1)	0.6420(4)	0.2539(3)	0.0311(9)
	6.56(5)	1	0.086(9)	0.6408(3)	0.2527(2)	0.041(1)

Site	*P*(GPa)	*s.o.f*	*x*	*y*	*z*	*Uiso*(Å^2)
O7	0.0001	1	0.4143(6)	0.7061(2)	-0.0103(1)	0.031(1)
	0.29(5)	1	0.4132(8)	0.7065(3)	-0.0112(2)	0.030(2)
	0.86(5)	1	0.412(1)	0.7071(3)	-0.0123(2)	0.031(2)
	1.00(5)	1	0.4096(8)	0.7073(3)	-0.0132(2)	0.034(2)
	1.26(5)	1	0.4083(8)	0.7081(3)	-0.0140(2)	0.032(2)
	1.62(5)	1	0.407(1)	0.7086(4)	-0.0148(2)	0.032(3)
	2.00(5)	1	0.3796(9)	0.1842(3)	0.4504(2)	0.0172(6)
	3.00(5)	1	0.3799(8)	0.1850(3)	0.4486(2)	0.0172(6)
	3.65(5)	1	0.3803(9)	0.1853(3)	0.4478(2)	0.0174(6)
	4.25(5)	1	0.3804(9)	0.1855(3)	0.4466(2)	0.0158(6)
	4.76(5)	1	0.379(1)	0.1859(3)	0.4457(2)	0.0166(6)
	5.83(5)	1	0.3795(9)	0.1860(5)	0.4442(2)	0.0169(6)
	6.56(5)	1	0.3808(8)	0.1867(3)	0.4438(2)	0.0211(2)
O8	0.0001	1	0.2241(7)	0.5335(2)	0.4324(2)	0.034(2)
	0.29(5)	1	0.2244(9)	0.5314(3)	0.4324(2)	0.036(3)
	0.86(5)	1	0.225(1)	0.5290(3)	0.4322(2)	0.035(3)
	1.00(5)	1	0.2259(9)	0.5281(3)	0.4324(2)	0.034(3)
	1.26(5)	1	0.228(1)	0.5272(3)	0.4325(2)	0.033(3)
	1.62(5)	1	0.229(1)	0.5252(5)	0.4327(3)	0.033(4)
	2.00(5)	1	0.303(1)	0.5571(5)	0.4783(4)	0.048(1)
	3.00(5)	1	0.300(1)	0.5606(5)	0.4766(4)	0.045(1)
	3.65(5)	1	0.298(1)	0.5615(5)	0.4755(4)	0.043(1)
	4.25(5)	1	0.298(1)	0.5627(5)	0.4754(3)	0.039(1)
	4.76(5)	1	0.298(1)	0.5635(5)	0.4751(3)	0.038(1)
	5.83(5)	1	0.296(1)	0.5644(4)	0.4738(3)	0.0359(9)
	6.56(5)	1	0.298(9)	0.5619(3)	0.4726(2)	0.048(3)
O9	0.0001	1	0.5651(5)	0.2727(2)	0.3629(1)	0.017(1)
	0.29(5)	1	0.5680(7)	0.2734(2)	0.3637(1)	0.015(2)
	0.86(5)	1	0.5711(7)	0.2739(2)	0.3645(2)	0.017(2)
	1.00(5)	1	0.5727(6)	0.2744(2)	0.3648(1)	0.015(2)
	1.26(5)	1	0.5741(7)	0.2744(2)	0.3651(2)	0.016(2)
	1.62(5)	1	0.577(1)	0.2738(3)	0.3654(2)	0.015(2)
	2.00(5)	1	0.3674(8)	0.2033(3)	0.0938(2)	0.0156(6)
	3.00(5)	1	0.3687(8)	0.2021(3)	0.0930(2)	0.0156(5)
	3.65(5)	1	0.3699(9)	0.2014(3)	0.0925(2)	0.0167(6)
	4.25(5)	1	0.3702(9)	0.2008(3)	0.0919(2)	0.0154(6)
	4.76(5)	1	0.372(1)	0.1999(3)	0.0917(2)	0.0159(1)
	5.83(5)	1	0.3744(9)	0.1989(3)	0.0909(2)	0.0171(6)
	6.56(5)	1	0.3730(7)	0.1963(2)	0.0894(1)	0.021(2)

Site	*P*(GPa)	*s.o.f*	*x*	*y*	*z*	*Uiso*(Å^2)
O10	0.0001	1	0.0391(6)	0.5624(3)	0.0856(1)	0.027(2)
	0.29(5)	1	0.042(1)	0.5633(3)	0.0850(2)	0.027(2)
	0.86(5)	1	0.043(1)	0.5652(3)	0.0842(2)	0.027(3)
	1.00(5)	1	0.0436(8)	0.5650(3)	0.0842(2)	0.029(2)
	1.26(5)	1	0.0465(9)	0.5653(3)	0.0833(2)	0.024(2)
	1.62(5)	1	0.048(1)	0.5670(5)	0.0828(3)	0.026(4)
	2.00(5)	1	-0.060(1)	0.4141(4)	0.0767(3)	0.0256(7)
	3.00(5)	1	-0.062(1)	0.4139(3)	0.0761(2)	0.0248(7)
	3.65(5)	1	-0.064(1)	0.4140(3)	0.0756(3)	0.0226(7)
	4.25(5)	1	-0.065(1)	0.4138(3)	0.0753(2)	0.0217(7)
	4.76(5)	1	-0.066(1)	0.4135(3)	0.0751(3)	0.0221(7)
	5.83(5)	1	-0.068(1)	0.4139(3)	0.0740(2)	0.0213(6)
	6.56(5)	1	-0.065(1)	0.4137(3)	0.0760(2)	0.024(2)
O11	0.0001	1	0.1654(6)	0.1170(2)	0.0766(1)	0.027(2)
	0.29(5)	1	0.1639(8)	0.1174(3)	0.0757(2)	0.029(2)
	0.86(5)	1	0.161(1)	0.1180(3)	0.0750(2)	0.028(2)
	1.00(5)	1	0.1609(8)	0.1170(3)	0.0742(2)	0.026(2)
	1.26(5)	1	0.1598(8)	0.1172(3)	0.0739(2)	0.028(2)
	1.62(5)	1	0.160(1)	0.1180(4)	0.0736(3)	0.027(3)
	2.00(5)	1	0.031(1)	0.8323(4)	0.0495(3)	0.0311(9)
	3.00(5)	1	0.029(1)	0.8336(4)	0.0491(3)	0.0314(8)
	3.65(5)	1	0.029(1)	0.8342(4)	0.0492(3)	0.0295(8)
	4.25(5)	1	0.027(1)	0.8352(4)	0.0488(3)	0.0284(8)
	4.76(5)	1	0.025(1)	0.8351(4)	0.0483(3)	0.0286(8)
	5.83(5)	1	0.024(1)	0.8356(4)	0.0483(3)	0.0275(8)
	6.56(5)	1	0.0270(8)	0.8358(3)	0.0470(2)	0.033(2)

Table S2: Details pertaining to the structure refinements of kernite as a function of pressure.

P (GPa)	0.0001	0.29(5)	0.86 (5)	1.00(5)	1.26 (5)	1.62(5)
min≤h≤max	-8 < h < 6	-6 < h < 7	-6 < h < 7	-6 < h < 7	-6 < h < 7	-6 < h < 7
min≤k≤max	-17 < k < 17	-17 < k < 17	-17 < k < 17	-17 < k < 17	-17 < k < 17	-17 < k < 17
min≤l≤max	-31 < l < 31	-31 < l < 31	-31 < l < 31	-31 < l < 31	-31 < l < 31	-30 < l < 31
Unique reflections	2139	2135	2092	2083	2062	2058
Observed reflections $I > 3\sigma(I)$	1440	1228	1194	1165	1201	1245
R_{int} (obs)	2.25	2.40	2.63	2.49	2.62	2.99
R_{int} (all)	2.52	2.80	3.04	2.96	3.01	3.36
R_1 (obs)	6.83	7.09	7.02	6.60	7.32	8.11
R_1 (all)	9.78	12.34	12.21	11.50	12.19	12.90
wR_1 (obs)	7.57	7.70	7.78	7.40	8.59	10.88
wR_1 (all)	7.97	9.25	9.98	8.74	9.69	13.50
Residuals (e^-/Å^3)	+0.90;-0.74	+0.76;-0.82	+0.91;-0.74	+0.68;-0.68	+0.76;-0.69	+1.01;-0.71

P (GPa)	2.00(5)	3.00 (5)	3.65 (5)	4.25(5)	4.76 (5)	5.83 (5)	6.56(5)
min≤h≤max	-6 < h < 7	-6 < h < 7	-6 < h < 7	-6 < h < 7	-6 < h < 7	-6 < h < 7	-6 < h < 7
min≤k≤max	-17 < k < 17	-18 < k < 18	-18 < k < 18	-18 < k < 18	-18 < k < 18	-17 < k < 18	-17 < k < 18
min≤l≤max	-28 < l < 28	-28 < l < 28	-28 < l < 28	-28 < l < 28	-28 < l < 28	-28 < l < 27	-28 < l < 27
Unique reflections	1883	1847	1831	1795	1778	1722	1712
Observed reflections $I > 3\sigma(I)$	1106	1082	1035	1037	1053	1008	581
R_{int} (obs)	2.60	3.37	3.48	1.97	2.58	3.89	6.00
R_{int} (all)	2.99	3.72	3.83	2.32	2.95	4.49	7.61
R_1 (obs)	9.68	9.11	9.29	8.95	9.02	9.96	9.86
R_1 (all)	16.19	14.78	15.25	14.77	14.37	15.68	18.81
wR_1 (obs)	10.16	9.65	10.15	9.64	9.56	10.54	12.01
wR_1 (all)	11.67	10.94	11.49	11.01	11.28	11.75	13.97
Residuals (e^-/Å^3)	+1.04;-0.89	+0.83;-0.78	+0.91;-0.89	+0.94;-0.78	+1.11;-0.86	+0.87;-0.84	+0.91;-0.71

Table S3: B-O distances (in Å) at different pressure.

P (GPa)	B2-O4	B2-O2	B2-O3	B2-O9	B3-O4	B3-O1	B3-O2	B3-O5
0.0001	1.434(3)	1.446(4)	1.524(7)	1.499(4)	1.439(4)	1.508(3)	1.458(3)	1.485(6)
0.29(5)	1.422(4)	1.440(5)	1.539(9)	1.497(5)	1.445(6)	1.494(4)	1.456(4)	1.483(8)
0.86(5)	1.428(4)	1.447(5)	1.522(9)	1.496(5)	1.445(6)	1.490(4)	1.454(5)	1.475(9)
1.00(5)	1.427(4)	1.448(5)	1.518(8)	1.498(4)	1.442(5)	1.493(4)	1.453(4)	1.475(8)
1.26(5)	1.431(4)	1.442(5)	1.523(9)	1.491(5)	1.430(6)	1.484(4)	1.456(5)	1.481(9)
1.62(5)	1.425(6)	1.441(7)	1.524(12)	1.490(7)	1.445(8)	1.484(6)	1.444(7)	1.476(12)
2.00(5)	1.443(5)	1.453(6)	1.492(11)	1.492(6)	1.439(8)	1.520(5)	1.418(5)	1.496(11)
3.00(5)	1.429(6)	1.453(8)	1.493(13)	1.499(7)	1.438(9)	1.518(6)	1.417(6)	1.490(12)
3.65(5)	1.435(5)	1.433(6)	1.498(11)	1.490(6)	1.433(8)	1.515(5)	1.418(6)	1.489(11)
4.25(5)	1.431(5)	1.435(7)	1.486(11)	1.496(6)	1.430(8)	1.508(5)	1.419(5)	1.491(11)
4.76(5)	1.428(5)	1.433(7)	1.491(11)	1.494(6)	1.433(8)	1.499(5)	1.417(5)	1.500(11)
5.83(5)	1.420(5)	1.441(6)	1.485(11)	1.490(6)	1.429(8)	1.510(5)	1.410(5)	1.485(10)
6.56(5)	1.438(8)	1.46(1)	1.48(2)	1.48(1)	1.44(1)	1.516(8)	1.410(9)	1.46(2)

P (GPa)	B4-O3	B4-O5	B4-O6	B1-O1	B1-O9	B1-O7
0.0001	1.362(6)	1.357(4)	1.381(8)	1.363(3)	1.351(4)	1.382(3)
0.29(5)	1.360(7)	1.358(5)	1.374(10)	1.357(4)	1.348(5)	1.385(4)
0.86(5)	1.370(8)	1.355(6)	1.383(12)	1.365(4)	1.345(5)	1.377(5)
1.00(5)	1.372(7)	1.358(5)	1.371(10)	1.364(4)	1.345(5)	1.378(4)
1.26(5)	1.367(8)	1.352(5)	1.380(11)	1.364(4)	1.346(5)	1.377(5)
1.62(5)	1.365(11)	1.370(7)	1.367(16)	1.367(6)	1.339(7)	1.383(7)
2.00(5)	1.338(10)	1.376(7)	1.391(14)	1.349(5)	1.351(7)	1.370(6)
3.00(5)	1.337(11)	1.377(7)	1.388(16)	1.346(6)	1.350(8)	1.369(7)
3.65(5)	1.338(10)	1.377(7)	1.388(14)	1.358(5)	1.341(7)	1.361(6)
4.25(5)	1.337(10)	1.374(6)	1.390(14)	1.349(5)	1.345(7)	1.369(6)
4.76(5)	1.338(9)	1.371(6)	1.383(14)	1.350(5)	1.349(7)	1.367(6)
5.83(5)	1.335(9)	1.375(6)	1.370(13)	1.351(5)	1.341(7)	1.364(6)
6.56(5)	1.37(2)	1.40(1)	1.31(2)	1.329(8)	1.36(1)	1.36(1)

Table S4: Magnitude and orientation of the Eulerian unit-strain ellipsoids, calculated between the maximum and minimum pressures of the stability field for each of the three polymorphs.

Unit-strain along the three principal axes of the ellipsoid [GPa^{-1}]	∠with *a*	∠with *b*	∠with *c*
0.0212(3)	46.4(6)	90	63.7(6)
0.0059(1)	42.2(1)	90	152.4(1)
0.0047(1)	90	0	90
	Kernite-I, calculated between 0.0001 and 1.60(5) GPa		
0.0100(2)	31(1)	90	83(1)
0.00507(9)	58.6(1)	90	173.8(1)
0.00182(4)	90	0	90
	Kernite-II, calculated between 2.00(5) and 6.56(5) GPa		
0.0065(5)	69(13)	90	47(13)
0.0041(7)	158(14)	90	43(14)
0.0028(1)	90	0	90
	Kernite-III, calculated between 7.51 (5) and 14.61 (5) GPa		